

Electronic Supplementary Information for “Characterizing the free-energy landscapes of DNA origamis”

Chak Kui Wong,[†] Chuyan Tang,[†] John S. Schreck,[‡] and Jonathan P. K. Doye^{*,†}

[†]*Physical and Theoretical Chemistry Laboratory, Department of Chemistry, University of Oxford, South Parks Road, Oxford, OX1 3QZ, UK*

[‡]*National Center for Atmospheric Research, Computational and Information Systems Laboratory, 850 Table Mesa Drive, Boulder, CO 80305, USA*

E-mail: jonathan.doye@chem.ox.ac.uk

Additional methodological details

oxDNA simulations We used the oxDNA coarse-grained model^{1,2} (Fig. S1) to perform molecular dynamics simulations of the DNA nanostructures. We used the second-generation version of the model (sometimes called “oxDNA2”);³ one of the improvements in this version of the model was a tuning of the potential parameters to better reproduce the structures of large DNA nanostructures. As we are concerned here with the fundamental properties of the free-energy landscapes and not any potential sequence dependence to them, we used the sequence-averaged version of the model in which the strength of the interactions are independent of the identity of the nucleotides involved (note base pairing still can only occur between complementary nucleotides).

Simulations were performed at 300 K using a Langevin thermostat. The time-step used was 0.005 in the internal simulation units of the oxDNA code, which corresponds to 15 fs. The solvent environment is treated implicitly as a dielectric continuum. We use a salt concentration of $[\text{Na}^+] = 1.0 \text{ M}$, which provides a reasonable representation of the high salt conditions typically used for DNA nanotechnology. Due to large system sizes, we use the GPU implementation of the oxDNA simulation code.⁴

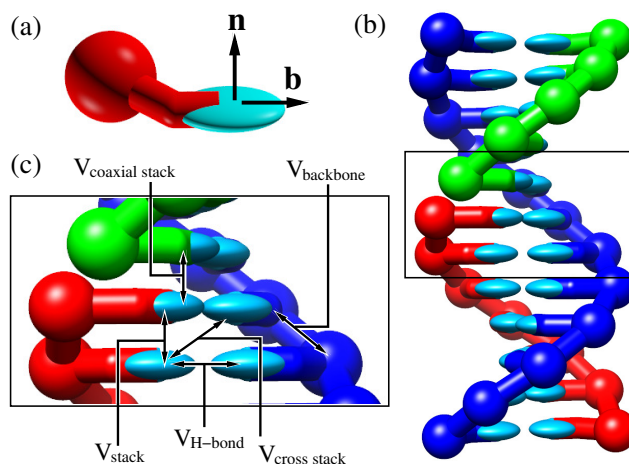


Figure S1: (a) An oxDNA nucleotide along with the “base” and “normal” vectors used to define its orientation. (b) A nicked double helix with 12 base pairs. (c) A close-up of the double helix illustrating some of the interactions in the oxDNA model.

To apply umbrella sampling in molecular dynamics simulations it is necessary to compute the contributions to the forces arising from the umbrella potential. This is straightforward for the continuous distance-based order parameters and the harmonic umbrella potentials that we use here.

Generating starting configurations We converted the caDNAno design files of the

origamis into oxDNA format using the tacoxDNA package.⁵ The converted configurations cannot serve as starting configurations for molecular dynamics simulations because of nucleotides experiencing large forces due to particle overlaps or extended bonds. Therefore, the potential energy of these configurations is first minimized for 200 steps using a steepest-descent algorithm, and then the configurations are relaxed in a molecular dynamics simulation using a modified backbone potential for 10^6 steps. After that, the extended bonds have typically returned to their normal lengths, and the configurations are ready for simulation using the standard oxDNA force field. All designs were equilibrated for a further 10^8 steps, corresponding to about 1.5 μ s.

Nanotube

1D Umbrella Sampling We used umbrella sampling⁶ to calculate the free-energy landscape as a function of the order parameter R_{ee} , the end-to-end distance of the nanotube. To avoid “end” effects associated with the greater splaying of the helices at the nanotube ends and their larger fluctuations, we defined the end-to-end distance as the distance between the centres of mass of two groups of nucleotides that are slightly in from the ends. For design 1, the two groups contain the nucleotides at positions 44–64 and 1010–1030 respectively. For designs 2 and 3, the two groups contain the nucleotides at positions 49–69 and 1204–1224 respectively. These nucleotides are highlighted in Fig. 1(a). The nucleotide positions are as defined in the caDNAno design (Fig. S2).

For each nanotube design, we performed a set of simulations where the order parameter was restrained with a harmonic potential in each sampling window. The range was from $R_{ee} = 0$ to $R_{ee} \approx 1.02 L_c^{\text{approx}}$, where L_c^{approx} is an estimate of the contour length of the nanotube that is obtained by multiplying the number of base pairs along the nanotube between the two centres of mass of the groups of nucleotides by the rise per base pair (0.34 nm).

Before performing the umbrella sampling simulations, we first prepared starting configura-

tions for each window using non-equilibrium “pulling” simulations. Starting from an equilibrated configuration restrained at $R_{ee} = L_c^{\text{approx}}$ with a harmonic bias potential of stiffness $k = 57.09$ pN/nm, the bent configurations were generated by gradually reducing the equilibrium position of the harmonic bias potential at a constant rate such that it reached zero after 10^8 steps. Configurations were outputted every 2×10^5 steps, resulting in a total of 500 configurations that were then used as the starting configurations for the same number of equally-spaced windows from $R_{ee} = 0$ to $R_{ee} = L_c^{\text{approx}}$. Similarly, for the stretched configurations, the equilibrium position of the harmonic potential was gradually increased at the same constant rate as above, until the nanotube was no longer stable. Configurations were also outputted every 2×10^5 steps, resulting in a total of 28, 27, and 37 configurations for designs 1, 2 and 3, respectively, that were used as the starting configuration of the same number of equally-spaced umbrella sampling windows.

The above configurations were then used as starting points for simulations in which the configurations were constrained by a harmonic umbrella potential of stiffness $k_{ee} = 17.12$ pN/nm centred at the value of R_{ee} corresponding to that window. The value of k_{ee} was chosen so that the probability distributions of R_{ee} for adjacent windows had significant overlap (Fig. S3). Each window was equilibrated for 10^6 steps before a production run of 10^7 steps. R_{ee} was outputted every 10^3 steps, giving 10^4 data points for each window. Using the biased probability distributions of R_{ee} in each window, we used the Weighted Histogram Analysis Method (WHAM)^{7,8} to calculate the unbiased free-energy landscape of the system as a function of R_{ee} .

The production runs were then repeated with the last configuration of the previous production run, and WHAM was performed on the new data to calculate the free-energy landscape again. This process was repeated until the new free-energy landscape was not statistically different from the previously calculated free-energy landscape. For the nanotubes considered here, four sets of production runs were

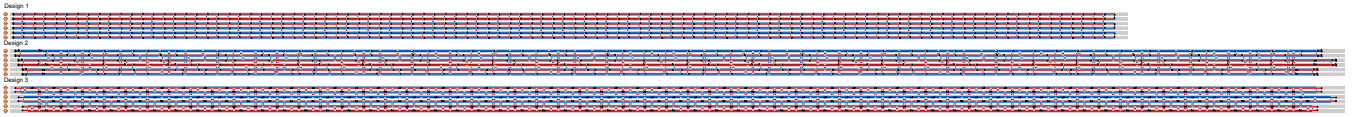


Figure S2: Full caDNAno designs for the three DNA nanotubes.

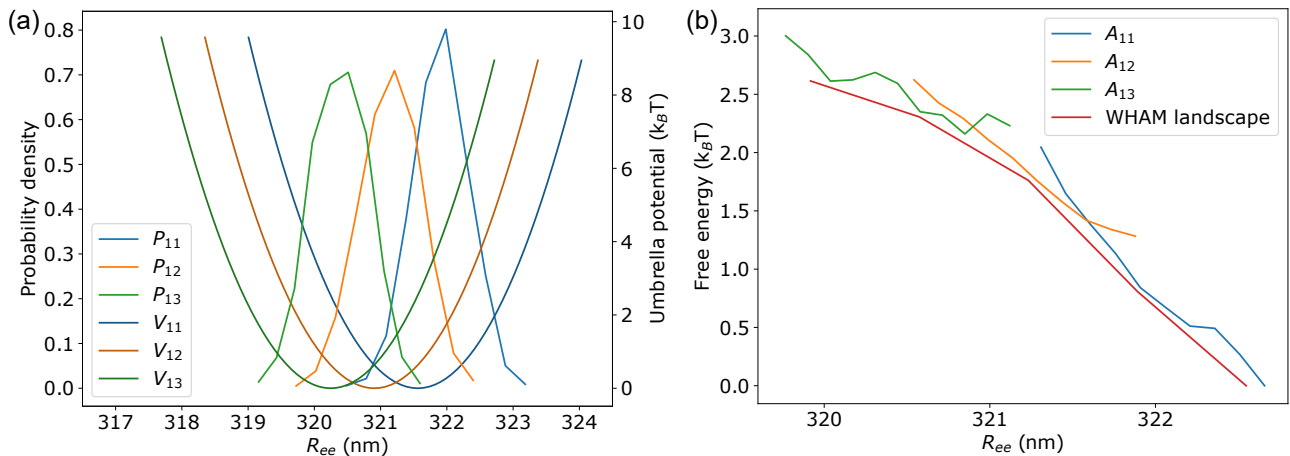


Figure S3: (a) Examples of the umbrella potentials $V_i(R_{ee})$ used for three windows for the bending of a DNA nanotube (design 1), and the probability distributions for those windows $p_i(R_{ee})$. i is the index of the umbrella sampling window. (b) From each probability distribution an estimate of the free-energy $A_i(R_{ee})$ can be obtained that will be most accurate for those R_{ee} values that are most well sampled in that simulation. If there is significant overlap between adjacent probability distributions an accurate best estimate of the overall free-energy landscape can be obtained using WHAM, as illustrated.

needed for convergence.

2D Umbrella Sampling To improve sampling in the transition region between the kinked and unkinked states of the nanotube, two-dimensional umbrella sampling was performed for design 1. The order parameters were chosen to be R_{ee} , the end-to-end distance of the nanotube defined previously, and R_{qq} , the distance between points one quarter and three quarters along the nanotube from the end points used for R_{ee} . Specifically, R_{qq} is defined as the distance between the centres of mass of another two groups of nucleotides, namely those nucleotides at positions 285–305 and 768–788, respectively. The nucleotide positions are as defined in the caDNAno design.

The sampling region chosen ranges from $R_{ee} = 148.0$ nm to $R_{ee} = 190.7$ nm, and $R_{qq} = 93.7$ nm to $R_{qq} = 139.7$ nm. Windows along R_{ee} had a spacing of 0.658 nm, which is the same as that used for the one-dimensional sam-

pling, and windows along R_{qq} had a spacing of 1.70 nm.

The final equilibrated configurations from the corresponding R_{ee} windows in the 1D umbrella sampling simulations were used as the starting configuration for each window. The simulations for each window were constrained by a two-dimensional harmonic potential centred at the values of R_{ee} and R_{qq} corresponding to that window. The harmonic bias potential had stiffness $k_{ee} = 17.12$ pN/nm and $k_{qq} = 1.71$ pN/nm in the R_{ee} and R_{qq} coordinates, respectively. Each window was equilibrated for 5×10^6 steps before a production run of 5×10^6 steps. After the production run, two-dimensional WHAM^{8,9} was performed to calculate the free-energy landscape in the transition region.

Combining 1D and 2D umbrella sampling To combine the free-energy landscape from one- and two-dimensional umbrella sampling of the SST design, we also recorded

R_{qq} in the one-dimensional sampling runs, but without any bias on this order parameter. We performed two-dimensional WHAM on the whole data set, but excluding the data from the one-dimensional sampling that overlapped with that from the two-dimensional sampling. The two-dimensional free-energy landscape was then projected onto R_{ee} to produce the new estimate of the one-dimensional landscape that is shown in Fig. 1.

Stretching We calculated the force-extension curve, $F(z)$, from our free-energy landscape, $A(R_{ee})$, using the following approach. Firstly, $F(z)$ can be related to $P(z)$ the probability distribution function for z :

$$\begin{aligned} F(z) &= -\frac{dA(z)}{dz} \\ &= -\frac{d(-k_B T \ln P(z))}{dz} \\ &= k_B T \frac{d \ln P(z)}{dz}, \end{aligned}$$

where $A(z)$ is the free energy as a function of z . Secondly, $P(z)$ can be related to $P(r)$ the probability distribution function of r

$$\begin{aligned} P(z) &= \frac{dC(z)}{dz} \\ &= \frac{d}{dz} \left(1 - \int_0^{2\pi} \int_0^{\arccos(\frac{z}{r})} \int_z^\infty P(r) r^2 \sin \theta dr d\theta d\phi \right) \\ &= \frac{d}{dz} \int_z^\infty P(r) 2\pi r^2 \left(\frac{z}{r} - 1 \right) dr \\ &= \int_z^\infty P(r) 2\pi r dr, \end{aligned}$$

where $C(z)$ denotes the cumulative distribution function for z . Finally, $P(r)$ can be related to $A(R_{ee})$:

$$P(r) = \frac{1}{4\pi r^2} \exp\left(\frac{-A(R_{ee})}{k_B T}\right).$$

Nanotube radius The average nanotube radius was calculated by averaging the radius at each slice (defined as the set of nucleotides with the same base-pair index in the caDNAno file)

along the nanotube, where each slice is separated by a single base-pair step:

$$\langle r_{\text{nanotube}} \rangle = \frac{1}{N_{\text{slice}}} \sum_{i=1}^{N_{\text{slice}}} r_{\text{nanotube}}(i).$$

The radius of the nanotube at a given slice is calculated by averaging the distances from the centre of each double helix to the centre of the nanotube for that slice:

$$r_{\text{nanotube}}(i) = \frac{1}{N_{\text{helix}}} \sum_{j=1}^{N_{\text{helix}}} |\mathbf{R}_{\text{duplex},j}(i) - \mathbf{R}_{\text{nanotube}}(i)|,$$

where the nanotube centre is simply defined as

$$\mathbf{R}_{\text{nanotube}}(i) = \frac{1}{N_{\text{helix}}} \sum_{j=1}^{N_{\text{helix}}} \mathbf{R}_{\text{duplex},j}(i).$$

Following Ref. 10 the centre of a double helix, $\mathbf{R}_{\text{duplex}}$, is defined as

$$\begin{aligned} \mathbf{R}_{\text{duplex}} &= \frac{1}{2} (\mathbf{r}_{\text{nuc1}} + \mathbf{r}_{\text{nuc2}}) \\ &\quad + \frac{\alpha}{2} (\hat{\mathbf{b}}_{\text{nuc1}} \times \hat{\mathbf{n}}_{\text{nuc1}} + \hat{\mathbf{b}}_{\text{nuc2}} \times \hat{\mathbf{n}}_{\text{nuc2}}) \end{aligned}$$

where \mathbf{r} , $\hat{\mathbf{b}}$, $\hat{\mathbf{n}}$ are the centre of mass position, the base unit vector, and the normal unit vector of the oxDNA nucleotide (Fig. S1), respectively, and $\alpha = 0.06$ (in the oxDNA simulation unit of length). The second term is a correction factor that takes into account that the centre of mass of the two nucleotides in an oxDNA base pair is slightly displaced towards the minor groove.

Relaxation of a bent nanotube For all three designs, an equilibrated configuration from the last umbrella sampling window ($R_{ee} = 0$) was used as the starting point. With the biasing umbrella potential removed the configuration was free to relax back to equilibrium with R_{ee} being used to monitor this relaxation. The simulation was run until the nanotube returned to its normal, relaxed length.

Origami sheets

2D Umbrella Sampling We used two-dimensional umbrella sampling to calculate the free-energy landscape as a function of the order parameters R_1 and R_2 , the two diagonal distances of the sheet. To avoid effects associated with the greater splaying of the helices at the edges of the sheet and the larger fluctuations at the corners, we defined each diagonal distance as the distance between the centres of mass of two groups of nucleotides that are slightly in from the corners. For the single-layer sheet, R_1 is the distance between nucleotides in helices 2–3 and positions 72–103, and those in helices 20–21 and positions 264–295; R_2 is the distance between nucleotides in helices 20–21 and positions 72–103, and those in helices 2–3 and positions 264–295. For the double-layer sheet, R_1 is the distance between nucleotides in helices 4–7 and positions 48–63, and those in helices 42–45 and positions 256–271; R_2 is the distance between nucleotides in helices 42–45 and positions 48–63, and those in helices 4–7 and positions 256–271. The helices and nucleotide positions are as defined in the caDNAno design (Fig. S4).

For each sheet design, we performed a set of simulations where the order parameters were restrained with a harmonic potential in each sampling window. The sampled ranges of the order parameter were from $R_1 = 0$ to $R_1 = R_{\max}$ and $R_2 = 0$ to $R_2 = R_{\max}$, where R_{\max} is the diagonal distance when the sheet is flat.

Before the umbrella sampling simulations, we prepared starting configurations for each window using pulling simulations. The sheets were first stretched diagonally outwards until they were flat to remove any initial bias towards the preferred curvature. Then, R_1 was restrained at R_{\max} with a harmonic bias potential of stiffness $k = 57.09$ pN/nm. The equilibrium position of the harmonic bias potential was gradually reduced at a constant rate such that it reaches zero after 10^8 steps. R_2 was similarly restrained during the pulling, but at a constant value of R_{\max} . Configurations were outputted every 10^6 steps, resulting in a total of 100 configurations. From each of these configura-

tions, a similar pulling simulation was performed on R_2 while R_1 was restrained at a constant value corresponding to that configuration. These pulling simulations generated starting configurations for 10 000 windows, each representing a point (R_1, R_2) on a square grid of 100 equally-spaced R_1 and R_2 values that run from 0 to R_{\max} .

After the starting configurations had been prepared, the simulations in each window were constrained by a 2-dimensional harmonic bias potential of stiffness $k = 17.12$ pN/nm centred at the value of R_1 and R_2 corresponding to that window. Each window was equilibrated for 10^6 steps before a production run of 10^6 steps. R_1 and R_2 was outputted every 10^3 steps, giving 10^3 data points for each window. The relatively short simulations were justified by the quick convergence of the data. For a smaller part of the landscape, we found that running the simulations for 10 times longer did not significantly alter the landscape.

Using the biased probability distributions of R_1 and R_2 in each window, we used 2D WHAM to calculate the unbiased free-energy landscape of the system. In total, 7500 windows were used for generating the free-energy landscape. Windows where both R_1 and R_2 are smaller than $R_{\max}/2$ were discarded because the configurations were too strained and severely deformed.

Curvature analysis The surface of the origami sheet can be represented parametrically in terms of the helix index (h) and base pair index (b) in the caDNAno design. Mathematically, the surface is given by $\mathbf{r}(h, b) = (X(h, b), Y(h, b), Z(h, b))$, where X , Y and Z are the splines of the respective coordinates fitted as a function of h and b . The principal curvatures, κ_1 and κ_2 , are the minimum and maximum values of the curvature at a given point on the surface. The mean curvature is given by $H = (\kappa_1 + \kappa_2)/2$ and the Gaussian curvature by $K = \kappa_1\kappa_2$.

To calculate these quantities at a given point

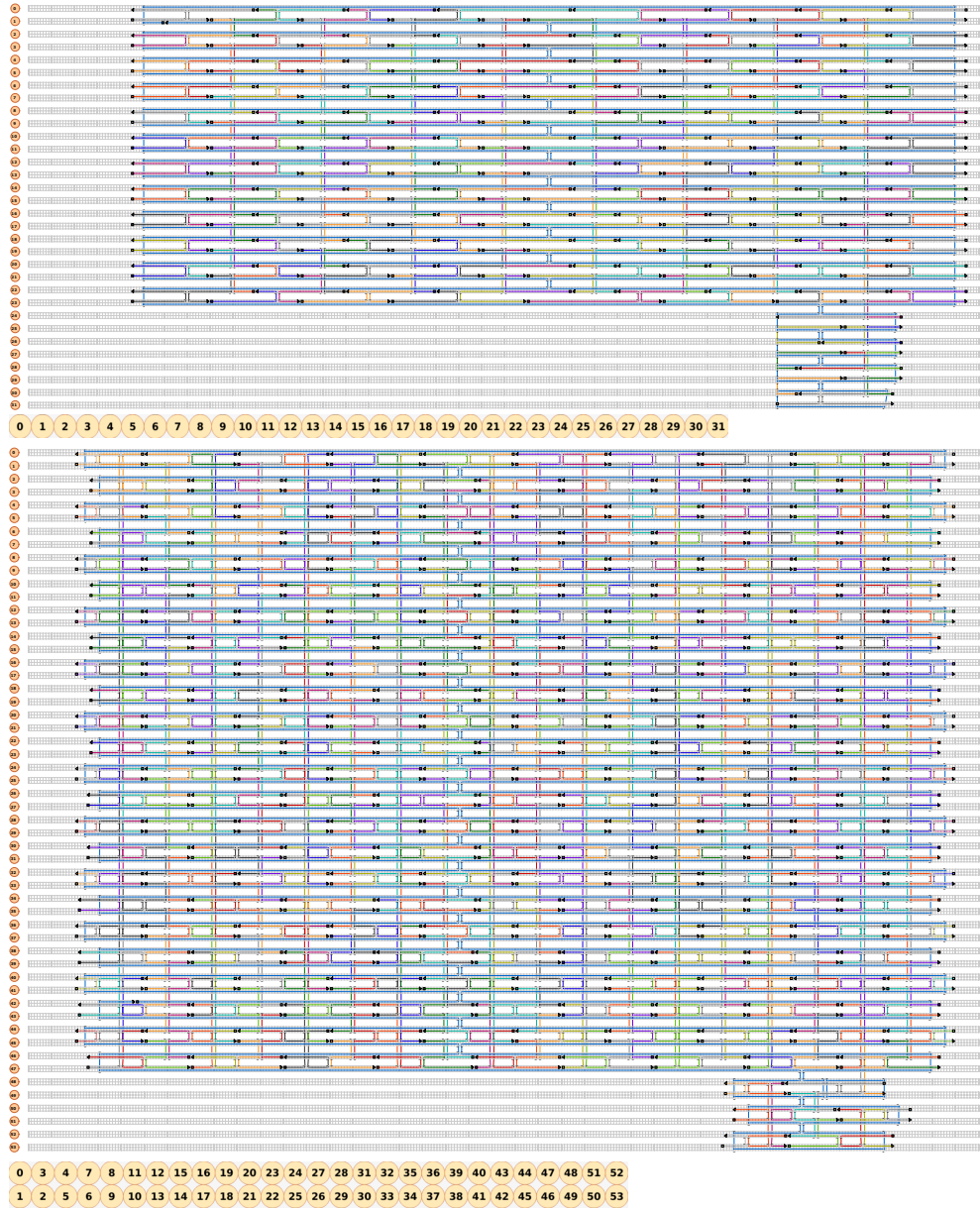


Figure S4: Full caDNAno designs for the single-layer and double-layer DNA origami sheets.

(h, b) on the sheet, we use the formulae¹¹ and

$$H = \frac{EN - 2FM + GL}{2(EG - F^2)}$$

$$K = \frac{LN - M^2}{EG - F^2}$$

where

$$\begin{aligned} E &= \mathbf{r}_h \cdot \mathbf{r}_h, & F &= \mathbf{r}_h \cdot \mathbf{r}_b, \\ G &= \mathbf{r}_b \cdot \mathbf{r}_b, & L &= \mathbf{r}_{hh} \cdot \hat{\mathbf{n}}, \\ M &= \mathbf{r}_{hb} \cdot \hat{\mathbf{n}}, & N &= \mathbf{r}_{bb} \cdot \hat{\mathbf{n}}, \end{aligned}$$

$$\begin{aligned} \mathbf{r}_h &= \frac{\partial \mathbf{r}}{\partial h}, & \mathbf{r}_b &= \frac{\partial \mathbf{r}}{\partial b}, \\ \mathbf{r}_{hh} &= \frac{\partial^2 \mathbf{r}}{\partial h^2}, & \mathbf{r}_{hb} &= \frac{\partial^2 \mathbf{r}}{\partial h \partial b}, \\ \mathbf{r}_{bb} &= \frac{\partial^2 \mathbf{r}}{\partial b^2}, & \hat{\mathbf{n}} &= \frac{\mathbf{r}_h \times \mathbf{r}_b}{|\mathbf{r}_h \times \mathbf{r}_b|}. \end{aligned}$$

For each system, the curvature calculations were done on a configuration averaged over an unbiased simulation trajectory started from the relevant free-energy minimum.

Twist measurement To measure the twist of the sheets we employ a similar approach to that used to define the distances R_1 and R_2 . We define vectors along the edges of either end of the sheet, and then measure the angle between those vectors after projection onto a plane perpendicular to a vector running along the centre of the sheet. Specifically, we use the same four centre-of-mass coordinates that were used to define R_1 and R_2 to define the ends of our edge vectors. The vector joining the midpoints of these two edge vectors is then used to define the vector along the centre of the sheet. As with R_1 and R_2 these positions are defined slightly in from the corners to avoid effects due to the greater splaying of the helices near the edges.

Further results

Kinking pathway Figure S5 provides example configurations illustrating the transition between the unkinked and kinked states for the design 1 nanotube at an R_{ee} value near to the midpoint of the kinking transition. The figure illustrates that kink formation and repair is a relatively slow process partly because it needs to be coupled to global changes in the nanotube configuration and that R_{qq} is a good order parameter to encourage that transition because it facilitates those global shape changes. For example, starting at the unkinked minimum it is unfavourable to introduce a kink at the centre because the stresses in other regions of the homogeneously bent tube would initially still remain. As R_{qq} is reduced the bending becomes more localized at the centre of the nanotube and the two arms either side of the centre become straighter. Below about $R_{qq} = 117$ nm, the bending is sufficiently localized near the centre that kink formation is favourable. As R_{qq} decreases further the stress in the rest of nanotube decreases as the two arms become straighter until the minimum corresponding to the unkinked state is reached.

Nanotube configurations Configurations of the design 1 nanotube at a number of values of R_{ee} were shown in the main text (Fig. 1). Here, in Figs. S6 and S7 we similarly illustrate

configurations of the design 2 and 3 nanotubes. Their reduced tendency to kink (compared to design 1) is apparent from the absence of kinks in the 153 nm example for design 2 and the 153 and 92 nm examples for design 3. The kinks in the design 2 nanotubes involve the unbinding of short 2-bp domains and perhaps also the end domain of a staple. By contrast, for the design 3 nanotubes the kinks involve the folding of the tube at the planes where each helix has a nick or a four-way junction, leading to the complete loss of the coaxial stacking at these sites.

Final configurations for each umbrella sampling window for the three designs are available to download from the Oxford University Research Archive.¹² We recommend such configurations are viewed using oxView.¹³

Interacting nucleotides Three types of interactions are counted, namely hydrogen bonding, stacking, and coaxial stacking (Fig. S1). A pair of nucleotides is considered as interacting through a particular interaction when the relevant interaction energy is lower than -2.49 kJ/mol. To produce the plots in Fig. S8, the total number of interacting pairs for each interaction type is counted for each configuration in the production trajectory in each umbrella sampling window, and averaged over each trajectory.

There are some common features in the plots of the R_{ee} -dependence of the number of interacting pairs for the three nanotube designs in Fig. S8. In the WLC regime of bending, the number of stacked pairs and base pairs remains fairly constant, while these numbers begin to decrease as a kink forms. Meanwhile, the number of coaxially stacked pairs decreases gradually even in the WLC regime; nicks and junctions are somewhat less stiff than intact double-stranded DNA and the enhanced bending at these sites leads to some loss of coaxial stacking. The numbers of stacked pairs and of base pairs show the clearest signals of kinking, with the most abrupt changes being observed for design 1. These can be correlated with the changes in R_{qq} seen in the plots in Fig. S9. Comparing the three nanotube designs, design 1 starts to kink at the largest R_{ee} and design 3 at the smallest

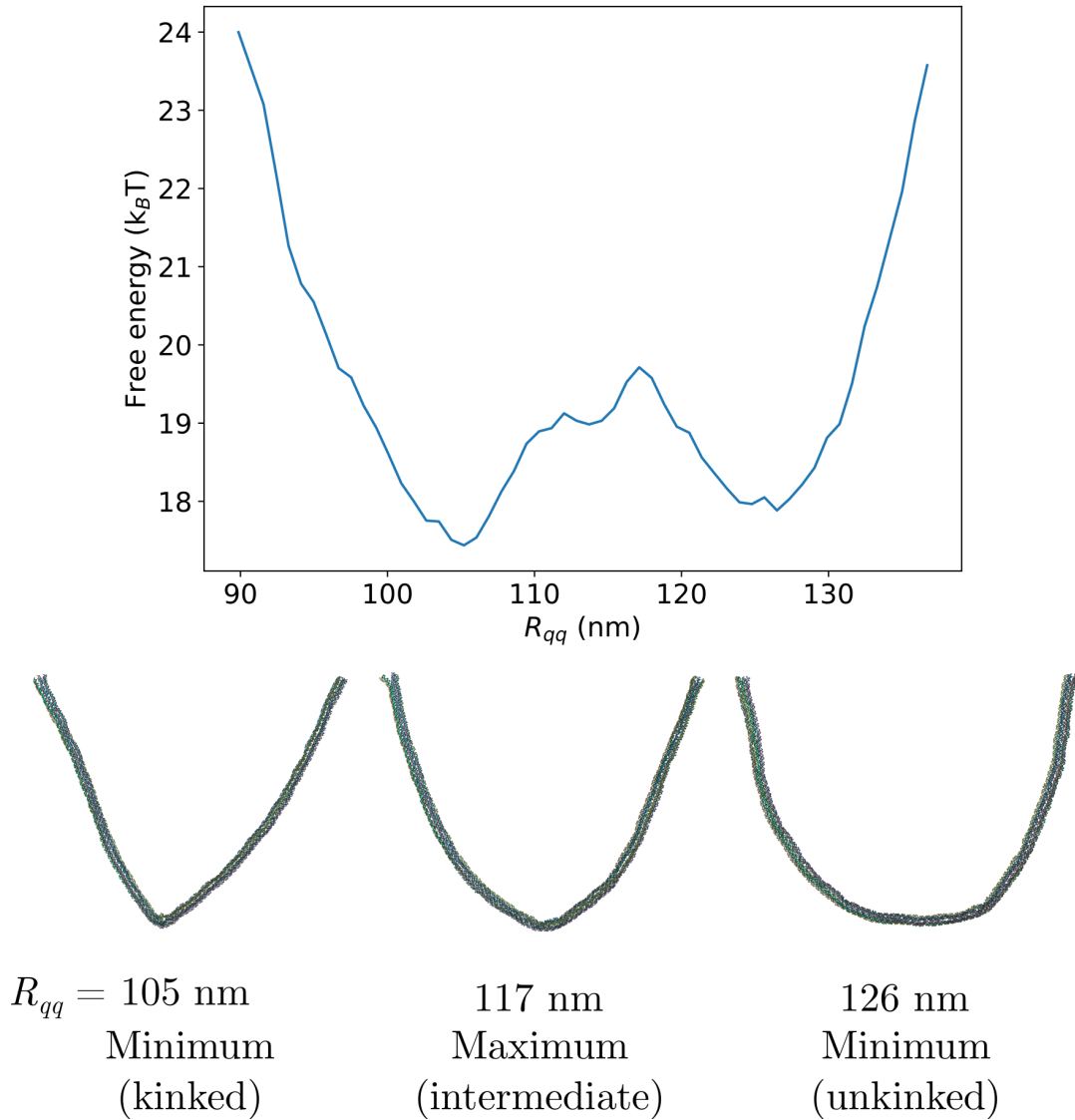


Figure S5: A cut through the two-dimensional free-energy landscape for the design 1 nanotube (Fig. 2 in the main text) at $R_{ee} = 170$ nm, which is near to the midpoint of the kink transition. Also depicted are representative configurations corresponding to the two minima and the top of the barrier in this profile.

R_{ee} .

For the stretched nanotubes, the number of stacked pairs and hydrogen bonds remains roughly constant, whereas the number of coaxially stacked pairs decreases sharply. This suggests that the junctions show greater compliance under tension than base pairs in the middle of a double helix. This effect may be coupled to the local structural changes at the junctions associated with the stretch-induced decrease in the nanotube radii.

For nanotubes released from a bent configuration, after they have fully relaxed, the num-

ber of interacting pairs is essentially the same as that of a normal unstressed nanotube (Table S1). This suggests that strong bending and kink formation do not induce irreversible structural changes in the nanotubes.

Force-dependent landscapes In the main text we showed how the free-energy landscape of nanotube 1 changes as a compressive force is applied along the end-to-end vector (Fig. 3). Here, we show the equivalent plots for the design 2 and 3 nanotubes (Fig. S10). The behaviour in the homogeneously-bent regime is

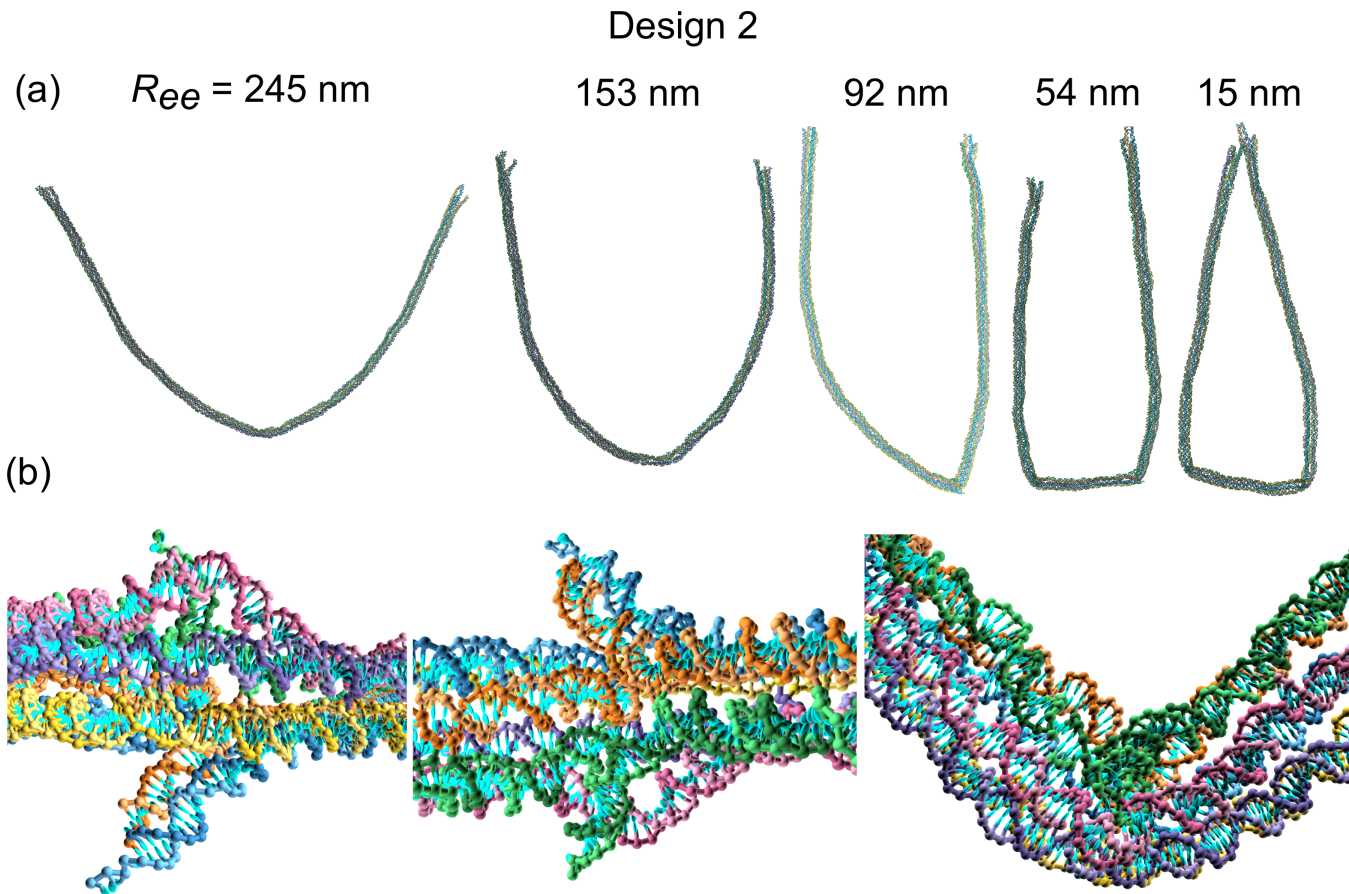


Figure S6: (a) Representative configurations of the design 2 nanotube at different values of R_{ee} . (b) Close-ups of the kink for the $R_{ee} = 92$ nm configuration. The view are from outside the kink (left), inside the kink (middle) and side-on (right).

Table S1: The average number of interaction pairs of different types for the three DNA nanotube designs. These are given for the relaxed nanotube at equilibrium and a nanotube that has been allowed to relax back towards equilibrium from an initially highly bent configuration in an unbiased simulation (i.e. the end configurations for the simulations represented in Fig. 6). In addition, the theoretical maximum values allowed by the design have been provided.

Design	State	Stacked pairs	Base pairs	Coaxially stacked pairs
1	at equilibrium	12233	6409	540
	bent and released	12232	6408	540
	theoretical maximum	12234	6426	606
2	at equilibrium	14383	7540	672
	bent and released	14384	7538	673
	theoretical maximum	14386	7560	722
3	at equilibrium	14036	7536	1020
	bent and released	14036	7536	1019
	theoretical maximum	14038	7560	1070

very similar to the design 1 nanotube. Namely, the free-energy landscape becomes very flat at the Euler critical buckling force, thus lead-

ing to a rapid change in R_{ee} expected for the homogeneously-bent state as the force goes above F_E . The precise values of the critical

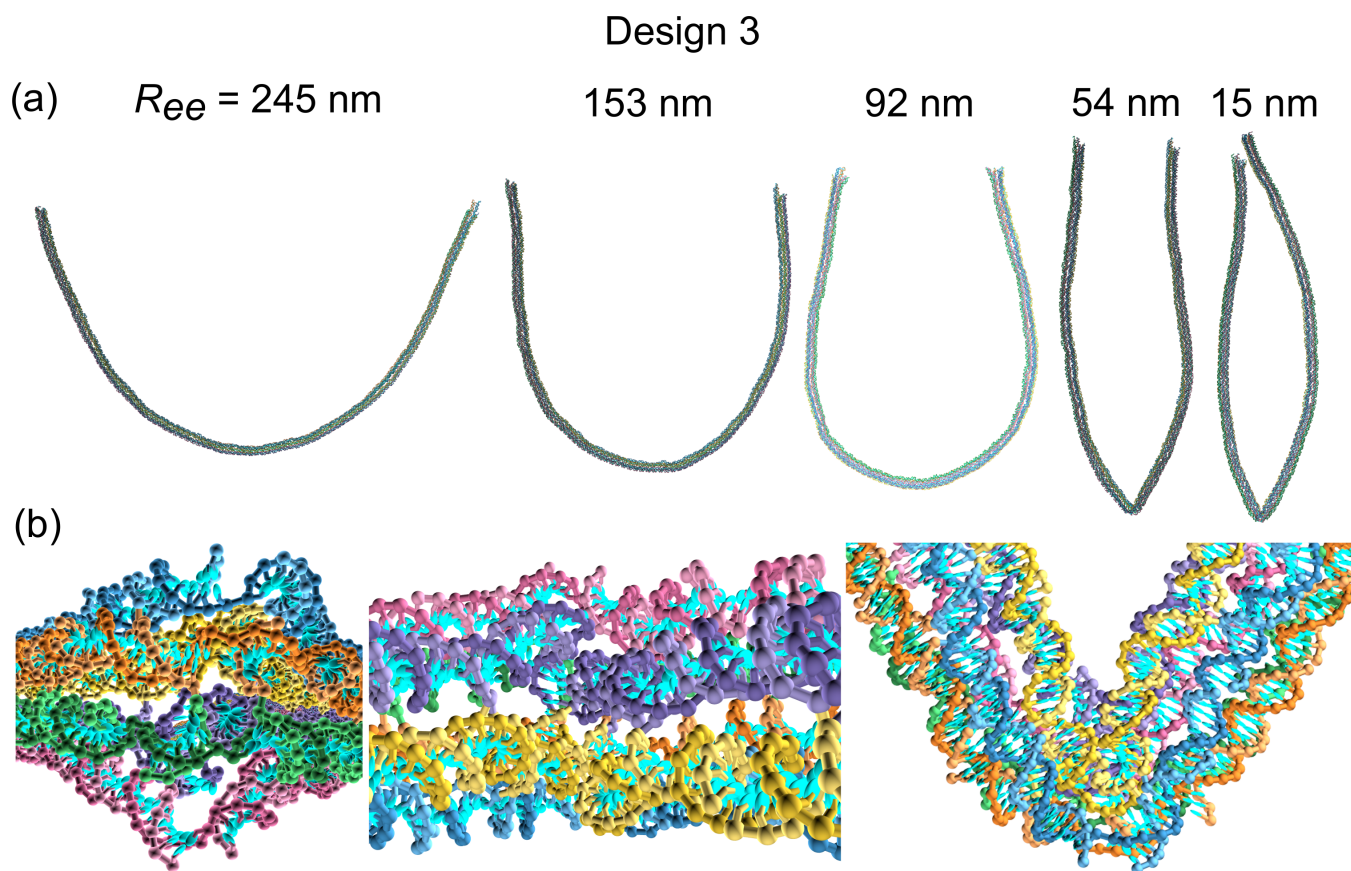


Figure S7: (a) Representative configurations of the design 3 nanotube at different values of R_{ee} . (b) Close-ups of the kink for the $R_{ee} = 54$ nm configuration. The view are from outside the kink (left), inside the kink (middle) and side-on (right).

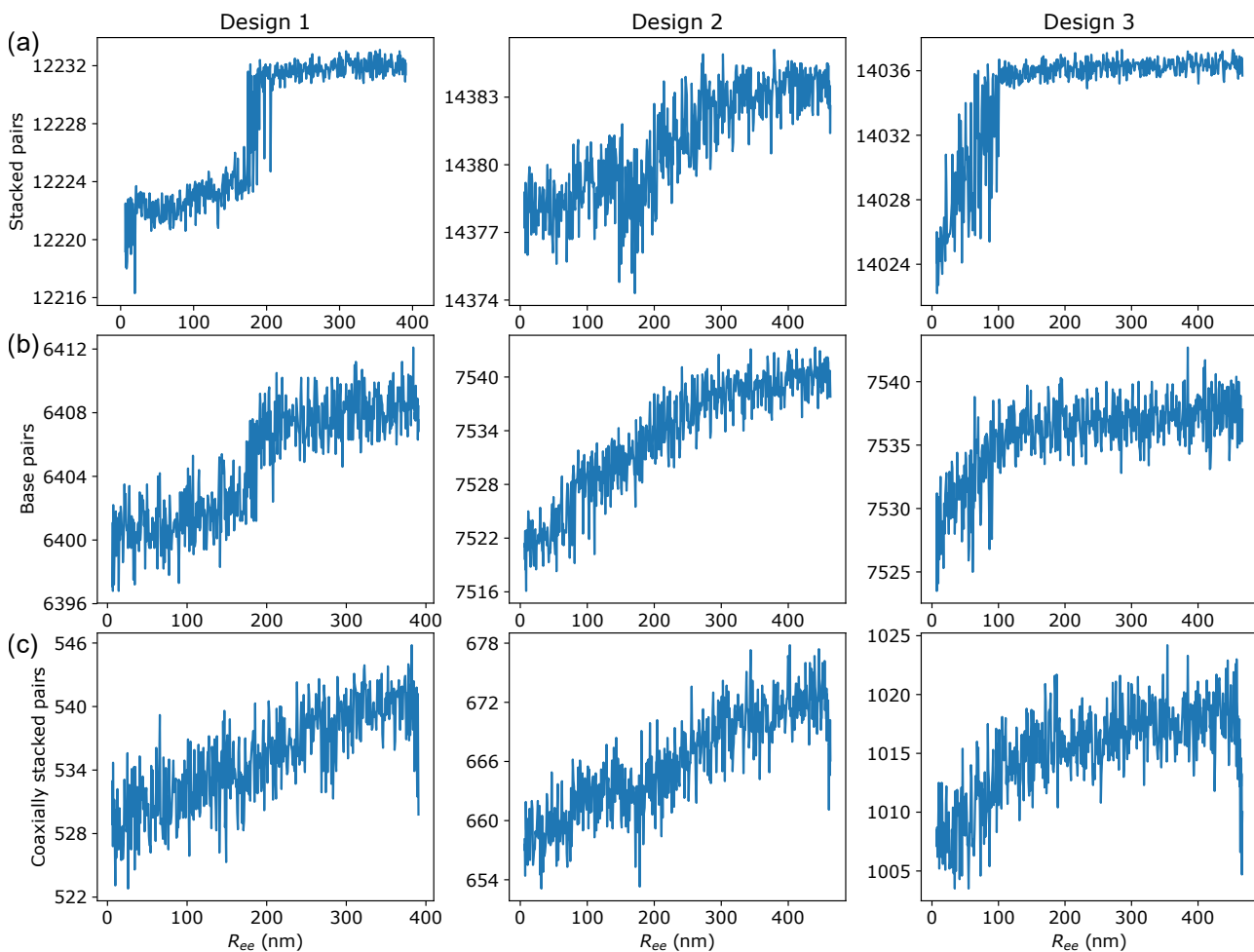


Figure S8: The total number of (a) pairs of stacked bases, (b) base pairs, and (c) coaxially-stacked pairs for the three DNA nanotube designs as a function of the end-to-end distance. Each point represents an average over one of the 500 umbrella sampling windows.

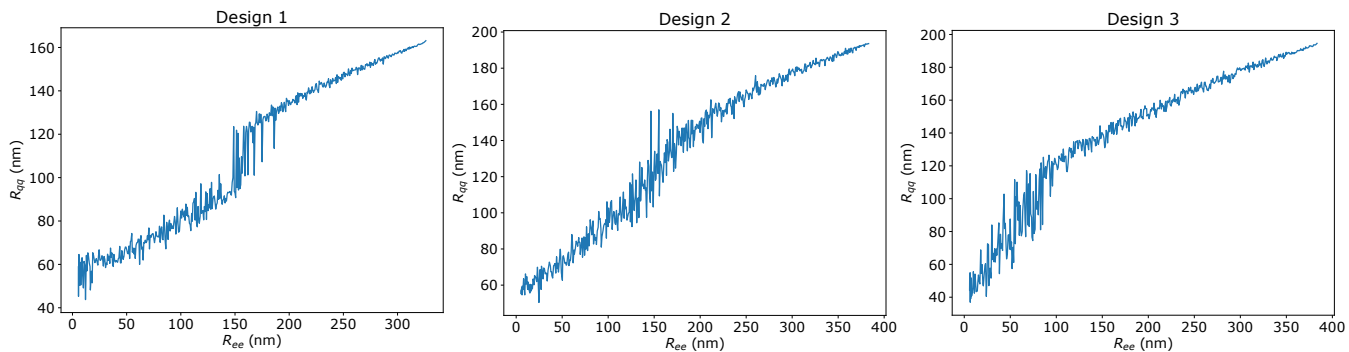


Figure S9: The $\frac{1}{4}-\frac{3}{4}$ distance (R_{qq}) as a function of the end-to-end distance (R_{ee}) for the three DNA nanotube designs. Each point represents an average over one of the 500 umbrella sampling windows.

buckling forces are different for all three systems due to their differences in persistence and contour lengths, as predicted by the formula given in the main text.

The main qualitative differences in behaviour between the three systems are due to their different propensities to kink. For the design 1 nanotube, the kinked state becomes lower in free energy than the unkinked state well before the critical buckling force is reached (Fig. 3). For the design 2 nanotube there is still a force range for which the kinked and unkinked states are both free-energy minima, but the force at which they are degenerate is now very close to F_E (at F_{kink} the barrier between the two states is $8.0 k_B T$). Finally, for design 3 the kinked state only becomes stable above F_E and at no point does the landscape have two free-energy minima separated by significant barrier. These changes are in part simply due to the larger contour length of these two nanotubes, which leads to a lowering of F_E , but the slope of the (zero-force) free-energy landscape in the kinked regime, i.e. the free-energy cost of further bending a kink, is also important as this determines the force at which the kinked state becomes a minimum.

DNA nanotube stretching In the main text we showed the force-extension curve for the design 1 nanotube as well as the change in radius of the nanotube on stretching (Fig. 6). Here, we provide similar plots for the design 2 and 3 nanotubes (Fig. S11). The behaviour is again very similar. The extensible worm-like chain model provides an excellent fit to the force-extension curves, and both nanotubes again show clear decreases in their radii in response to their stretching.

WLC fits The parameters for the WLC fits to $p(R_{ee})$ using the form given in Ref. 14 are given in Table S2 for the three nanotube designs. The parameters for the extensible WLC fits to the force-extension curves using the form given in Ref. 15 are given in Table S3 for the three nanotube designs. The values obtained for the contour lengths from the two methods are consistent albeit with a much greater degree

of precision available from the force-extension curves. Similarly, the values obtained for the persistence length are consistent. In this case, because the persistence lengths are much larger than the contour length, the force-extension curves provide much lower precision estimates of the persistence length.

For six DNA double helices stretched in parallel the extensional modulus would be expected to be six times the stretch modulus of the individual helices,¹⁰ i.e. $6 \times 2700 \text{ pN} \approx 16\,000 \text{ pN}$. However, due mainly to the change in the geometry of the crossovers linking the helices on stretching the extensional moduli of the nanotubes are instead about $10\,000 \text{ pN}$. The loss of about 1% of the coaxial stacking interactions on stretching (Fig. S8) may also play a small role in this reduction.

Gaussian curvature of sheets In Fig. S13 we show the Gaussian curvature, which is the product of the principal curvatures, for the origami sheets. For the double-layer sheet, as expected from its saddle-like shape, it has a negative Gaussian curvature across the whole sheet; the Gaussian curvature is fairly constant in the centre of the sheet, but increases in magnitude towards the corners. For the two free-energy minima of the single-layer sheet, like for the mean curvature shown in Fig. 7(d) in the main text, there is an approximate symmetry with respect to the “unperturbed” diagonal. For both forms, there are zones of strong positive Gaussian curvature (the principle curvatures have the same sign) that correspond to the areas with greatest mean curvature. Along the unperturbed diagonal, the curvature is close to zero in the centre leading to a near-zero Gaussian curvature, but at the corners of this diagonal the curvature along the diagonal becomes opposite to the prevailing curvature, leading to strongly negative Gaussian curvature. The latter is evident in the configurations visualized in Fig. 7(c).

Sheet twist The overall twist of the one-layer sheet is measured to be 84.2° and 85.1° for the free-energy minima A and B, respectively. The twist of the double-layer sheet is 43.6° . The

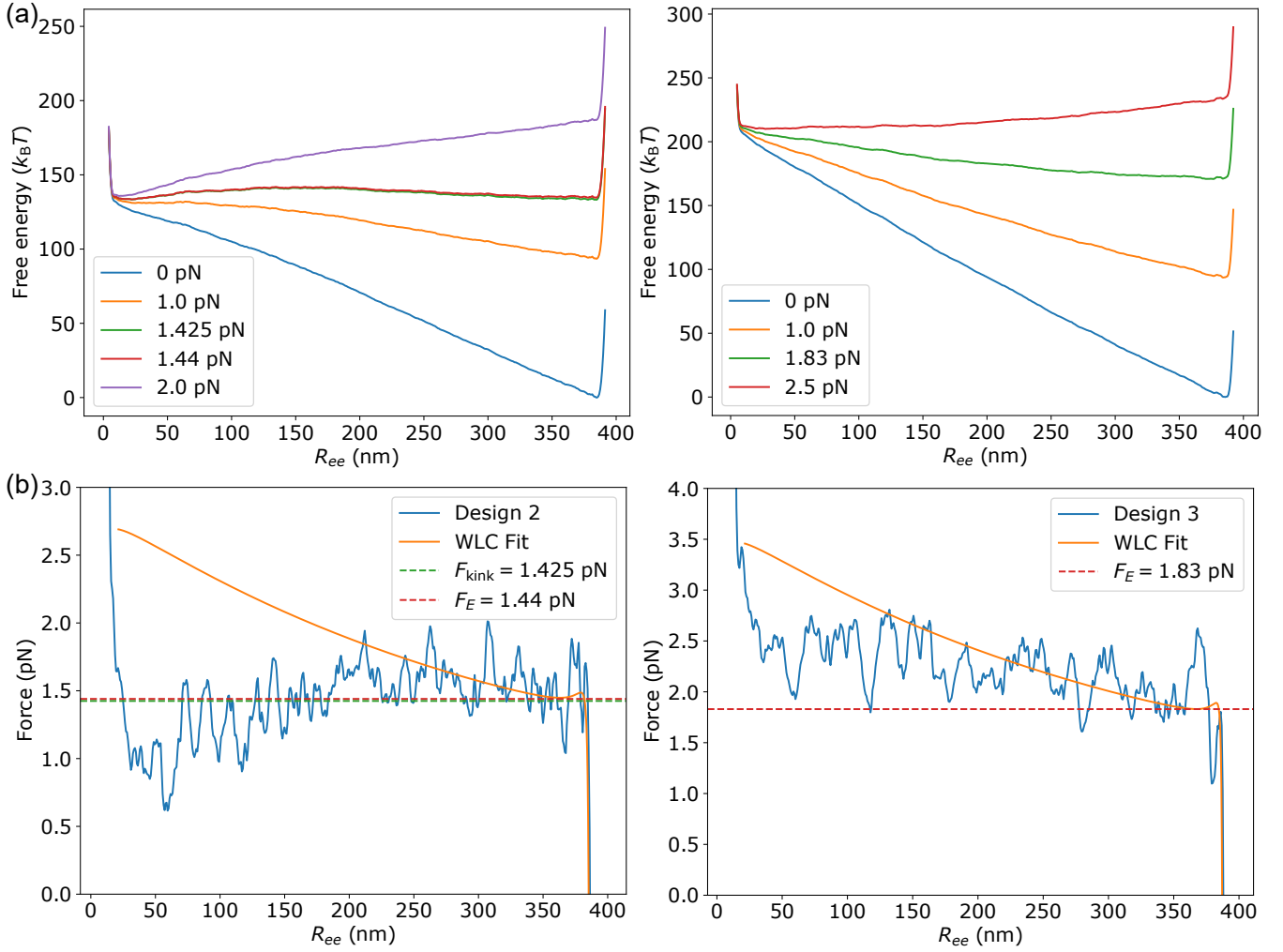


Figure S10: (a) The free-energy landscape for the design 2 and design 3 nanotubes at a series of compressive forces along the end-to-end vector. (b) $F(R_{ee}) = -dA(R_{ee})/dR_{ee}$ for the computed landscapes and their WLC fits. The horizontal lines correspond to the force at which the two free-energy minima associated with the kinked and unkinked states are degenerate (design 2 only) and the predicted Euler buckling critical force.

Table S2: Parameters for the WLC fit to probability distribution for the end-to-end distance for the three DNA nanotube designs. L_c is the contour length.

	L_c (nm)	L_p (μm)
Design 1	325 ± 5	6.49 ± 0.14
Design 2	388 ± 6	5.30 ± 0.13
Design 3	389 ± 9	6.77 ± 0.24

Table S3: Parameters for the extensible WLC fit to the force-extension curves of the three DNA nanotube designs.

	K (pN)	L_c (nm)	L_p (μm)
Design 1	10077 ± 150	325.20 ± 0.08	5.63 ± 0.48
Design 2	9147 ± 89	387.73 ± 0.07	5.00 ± 0.46
Design 3	10454 ± 62	388.93 ± 0.06	6.07 ± 0.74

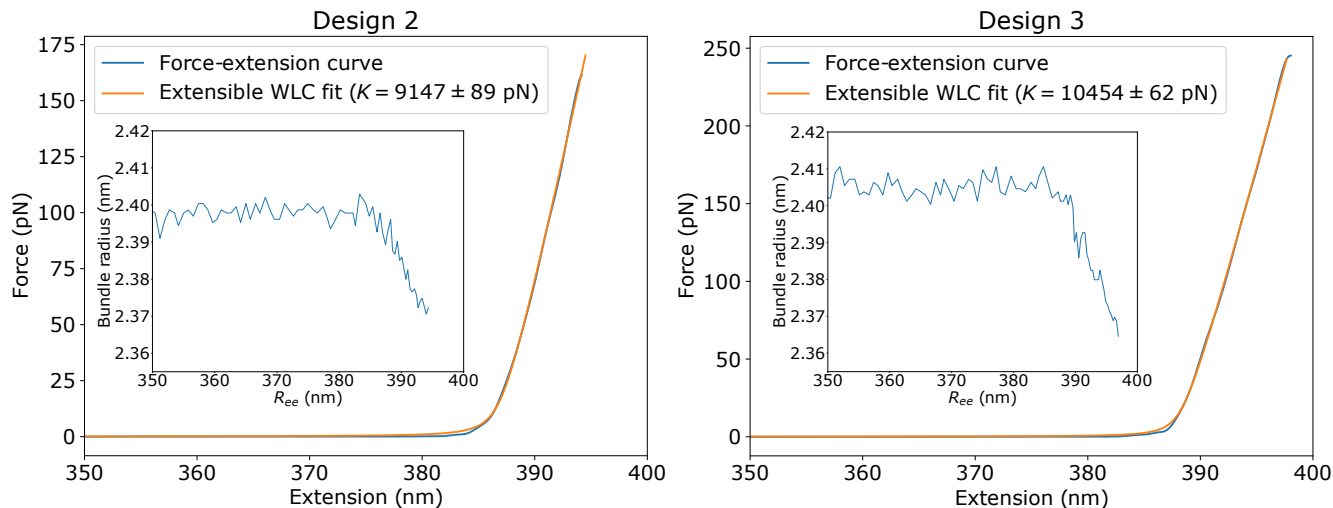


Figure S11: Force-extension curves for the DNA nanotube designs 2 and 3 along with extensible WLC fits (the fit parameters are given in Table S3). The insets show the average nanotube radius as a function of R_{ee} .

lower value of twist in the double-layer case is mainly due to its increased stiffness compared to the single-layer case.

References

- Ouldrige, T. E.; Louis, A. A.; Doye, J. P. K. Structural, Mechanical, and Thermodynamic Properties of a Coarse-Grained DNA Model. *J. Chem. Phys.* **2011**, *134*, 085101.
- Šulc, P.; Romano, F.; Ouldrige, T. E.; Rovigatti, L.; Doye, J. P. K.; Louis, A. A. Introducing Sequence-Dependent Interactions into a Coarse-Grained DNA Model. *J. Chem. Phys.* **2012**, *137*, 135101.
- Snodin, B. E. K.; Randisi, F.; Mosayebi, M.; Šulc, P.; Schreck, J. S.; Romano, F.; Ouldrige, T. E.; Tsukanov, R.; Nir, E.; Louis, A. A.; Doye, J. P. K. Introducing Improved Structural Properties and Salt Dependence into a Coarse-Grained Model of DNA. *J. Chem. Phys.* **2015**, *142*, 234901.
- Rovigatti, L.; Šulc, P.; Reguly, I. Z.; Romano, F. A Comparison between Parallelization Approaches in Molecular Dynamics Simulations on GPUs. *J. Comput. Chem.* **2015**, *36*, 1–8.
- Suma, A.; Poppleton, E.; Matthies, M.; Šulc, P.; Romano, F.; Louis, A. A.; Doye, J. P. K.; Micheletti, C.; Rovigatti, L. TacoxDNA: a User-Friendly Web Server for Simulations of Complex DNA Structures, from Single Strands to Origami. *J. Comput. Chem.* **2019**, *40*, 2586–2595.
- Torrie, G.; Valleau, J. Nonphysical Sampling Distributions in Monte Carlo Free-Energy Estimation: Umbrella sampling. *J. Comput. Phys.* **1977**, *23*, 187–199.
- Kumar, S.; Rosenberg, J. M.; Bouzida, D.; Swendsen, R. H.; Kollman, P. A. The Weighted Histogram Analysis Method for Free-Energy Calculations on Biomolecules. I. The Method. *J. Comput. Chem.* **1992**, *13*, 1011–1021.
- Grossfield, A. WHAM: the Weighted Histogram Analysis Method. http://membrane.urmc.rochester.edu/wordpress/?page_id=126, Version 2.0.9.
- Kumar, S.; Rosenberg, J. M.; Bouzida, D.; Swendsen, R. H.; Kollman, P. A. Multidimensional Free-Energy Calculations Using

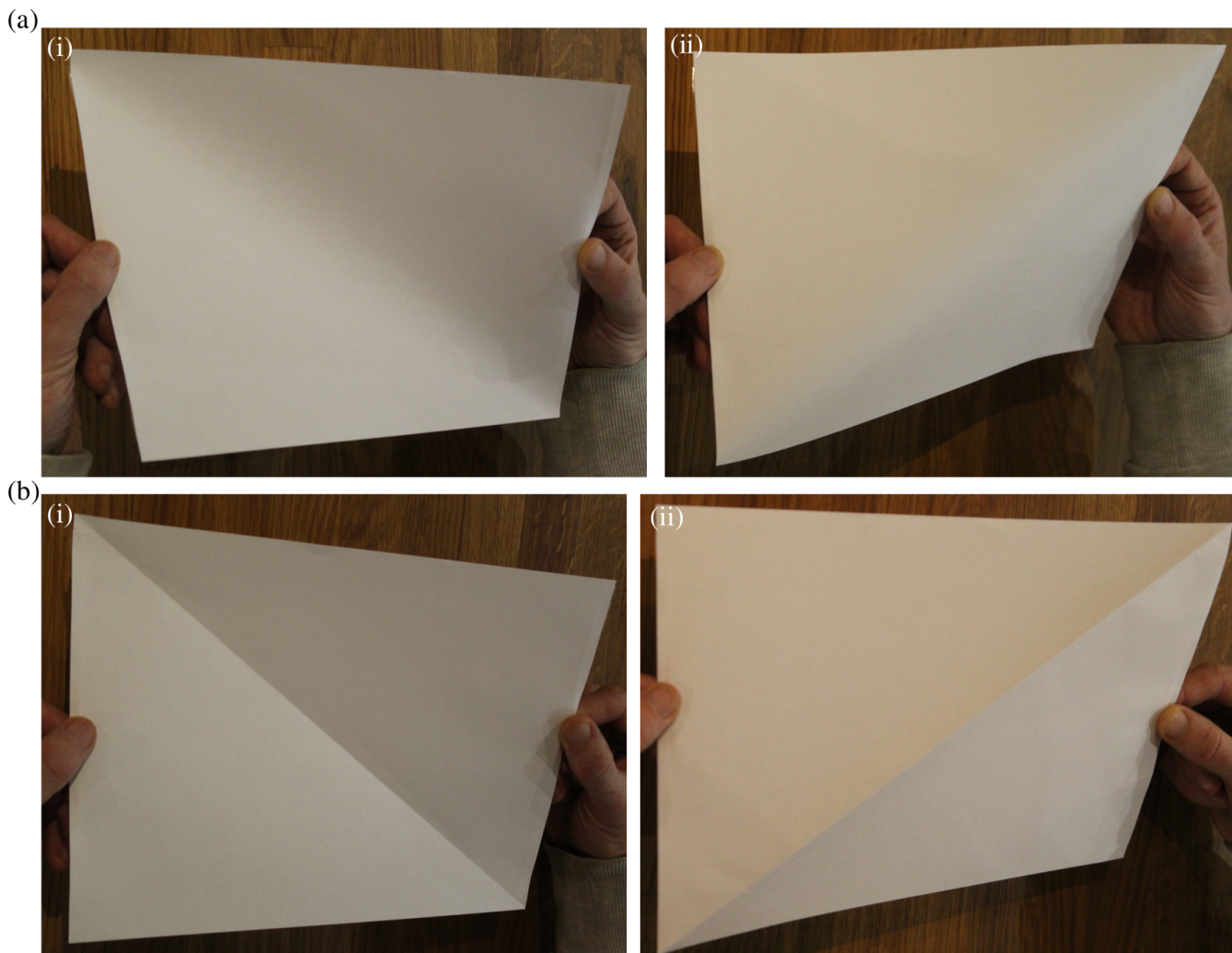


Figure S12: Images of right-twisted A4 sheets of paper. In (a) the curvature is continuous, whereas in (b) the curvature is localized at a fold. In (i) the bending is around the top-left to bottom-right diagonal and the curvature is positive, whereas in (ii) the bending is around the bottom-left to top-right diagonal and the curvature is negative. (b)(i) corresponds to a valley fold and (b)(ii) to a mountain fold.

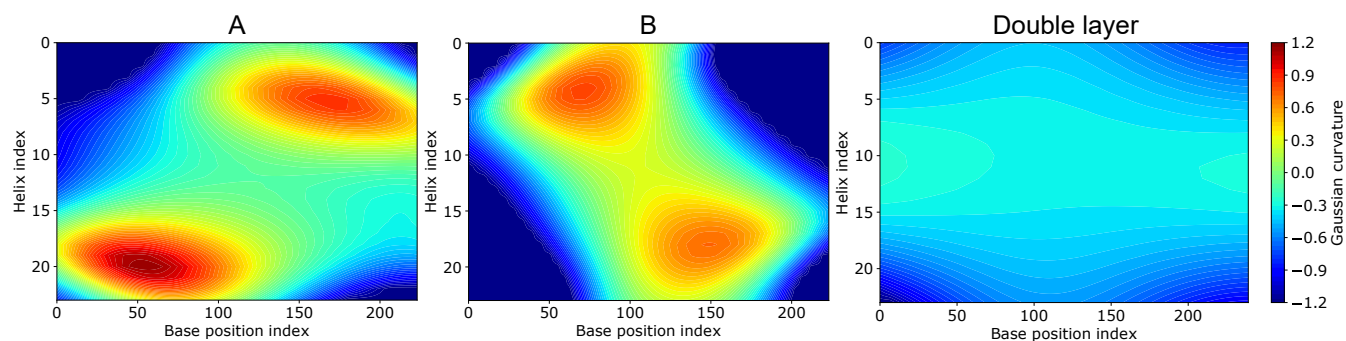


Figure S13: The Gaussian curvature of configurations at the two free-energy minima of the single-layer sheet and the free-energy minimum of the double-layer sheet as a function of the base-pair position within the sheet.

the Weighted Histogram Analysis Method. *J. Comput. Chem.* **1995**, *16*, 1339–1350.

10. Chhabra, H.; Mishra, G.; Cao, Y.; Prešern, D.; Skoruppa, E.; Tortora, M. M. C.; Doye, J. P. K. Computing the Elastic Mechanical Properties of Rodlike DNA Nanostructures. *J. Chem. Theory Comput.* **2020**, *16*, 7748–7763.
11. Gray, A.; Abbena, E.; Salamon, S. *Modern Differential Geometry of Curves and Surfaces with Mathematica, Third Edition (Studies in Advanced Mathematics)*; Chapman & Hall/CRC, 2006.
12. <https://ora.ox.ac.uk/objects/uuid:e9bc2712-82d5-4cc5-a656-dffd23438ca3>.
13. Poppleton, E.; Bohlin, M., J. Matthies; Sharma, S.; Zhang, F.; Šulc, P. Design, optimization, and analysis of large DNA and RNA nanostructures through interactive visualization, editing, and molecular simulation. *Nucleic Acids Res.* **2020**, *48*, e72.
14. Becker, N. B.; Rosa, A.; Everaers, R. The Radial Distribution Function of Worm-Like Chains. *Eur. Phys. J. E* **2010**, *32*, 53–69.
15. Odijk, T. Stiff Chains and Filaments under Tension. *Macromolecules* **1995**, *28*, 7016–7018.